Detecting and Localizing Open-Circuit Switch Faults in MMCs Using a Model Informed Estimation Scheme With Low Computational Complexity

Haoran Wang, *Graduate Student Member, IEEE*, Anjana Wijesekera, *Graduate Student Member, IEEE*, Gregory J. Kish, *Senior Member, IEEE*, and Qing Zhao, *Member, IEEE*

***Abstract*—The detection and localization of switch open-circuit faults (OCFs) in modular multilevel converters (MMCs) is crucial for enhancing their reliability. This article presents a model informed estimation-based fault detection and localization (FDL) scheme with low computational burden and implementation complexity. Its main novelty comprises two parts: derivation of a new model that quantifies the expected deviation in submodule capacitor voltages due to OCFs, and utilization of a Disturbance Observer (DOB) that, by leveraging the derived model, needs only one signature waveform for each arm. As a result, the proposed FDL scheme enables estimation of OCFs while maintaining very low and constant computational burden and implementation complexity regardless of the number of installed submodules per arm. To the best of the authors' knowledge, this work is the first to explore the use of OCFs models that can quantify the OCFs-induced deviations in the MMC capacitor voltages. Experimental results verify that the proposed model-informed FDL scheme with DOB can detect and localize OCFs accurately and rapidly, while retaining important traits such as robustness to load changes and measurement noise.**

***Index Terms*—Fault detection, fault localization, modular multilevel converters (MMCs), open-circuit fault, switch faults.**

I. Introduction

MODULAR multilevel converters (MMCs) offer notable advantages including modular and scalable structure, a compact footprint, and reduced filtering needs. These benefits stem from the modular design featuring series-stacked submodules (SMs) [1]. Leveraging these advantages, MMCs are playing progressively more significant roles in medium to high-voltage power applications. These applications encompass a wide array of fields including medium-voltage dc transmission, high-voltage dc transmission, energy storage systems, and static synchronous compensators [2], [3], [4], [5].

Received 1 August 2024; revised 4 October 2024 and 30 October 2024; accepted 6 November 2024. Date of publication 12 November 2024; date of current version 26 December 2024. This work was supported in part by the Natural Sciences and Engineering Research Council (NSERC) of Canada under Grant ALLRP 549804-19, in part by Alberta Electric System Operator, in part by AltaLink, in part by ATCO Electric, in part by ENMAX, in part by EPCOR Inc., and in part by FortisAlberta. Recommended for publication by Associate Editor A. R. Dekka. *(Corresponding author: Qing Zhao.)*

The authors are with the Department of Electrical and Computer Engineering, University of Alberta, Edmonton, AB T6G 2R3, Canada (e-mail: haoran16@ualberta.ca; awijesek@ualberta.ca; gkish@ualberta.ca; qingz@ualberta.ca).

Color versions of one or more figures in this article are available at https://doi.org/10.1109/TPEL.2024.3496532.

Digital Object Identifier 10.1109/TPEL.2024.3496532

Nevertheless, semiconductor power devices are recognized as the most vulnerable components in power electronic applications. The extensive use of semiconductor power devices in MMCs introduces numerous potential failure points [6]. A fault occurring in the semiconductor power devices may lead to unexpected shutdown of the entire system, resulting in higher system operation costs and severe safety concerns [7]. Therefore, it is of great importance to improve fault detection and localization (FDL) schemes to increase the reliability of MMC systems.

There are two main types of switch faults in MMCs: 1) open-circuit faults (OCFs); and 2) short-circuit faults. The short-circuit faults can be detected and handled by built-in short-circuit protections rapidly since they can lead to obvious over current [8]. However, OCFs do not result in immediate damage and can even remain undetected for several fundamental frequency cycles. If not detected in time, OCFs might cause secondary damage to the converter and even lead to system failure. Also in certain applications, such as high voltage dc transmission, the maintenance cycle of the MMC may exceed a year, during which faulty SMs cannot be replaced until the scheduled maintenance period. As a result, the MMC is expected to maintain uninterrupted operation until the faulty SMs can be replaced [9]. Therefore, it is necessary to detect, localize, and isolate the faulty SMs as soon as possible.

Existing works on FDL of switch OCFs in MMCs can be categorized into hardware-based and software-based schemes. Hardware-based schemes, as outlined in [10] and [11], offer rapid and accurate FDL. However, they often necessitate additional measurement circuits, thereby increasing both complexity and capital costs. Alternatively, in [12], sensors originally intended for measuring capacitor voltages of SM are relocated. While this approach reduces additional financial costs, labor costs remain significant in high-voltage MMCs with high SM counts. Wang and Peng [13] proposed a FDL scheme with reduced capacitor voltage sensors by grouping SMs. This approach substantially reduces the total number of voltage sensors needed relative to conventional MMC designs. However, the computational burden for the FDL scheme may remain considerable in high-voltage applications where hundreds of SMs per arm can result in many groups, each requiring a Kalman filter implementation for SM capacitor voltage estimation.

Compared to hardware-based schemes, software-based schemes are more widely adopted due to their cost-effectiveness.

Several software-based schemes have been proposed and validated for effectively detecting and localizing OCFs in MMCs [14], [15], [16], [17], [18], [19], [20], [21], [22], [23], [24], [25], [26], [27], [28], [29], [30], [31]. However, several research gaps still remain. The first research gap concerns complexity. Many of these existing schemes, such as [15], [16], [17], [19], [20], and [28], may impose increasing computational burdens or involve complex implementations, particularly for practical high-voltage applications where hundreds of SMs are installed in each arm. This is because these schemes typically require computations on all individual SMs at each sampling instant. To address the issue of heavy computational burden in MMCs with high SMs count, a recent study by [23] introduced a FDL scheme that maintains consistently low computational complexity regardless of the SMs count used per arm. It utilizes the signal synthesis technique on only two signature waveforms instead of executing the FDL algorithm on all individual SMs at each sampling instant. However, the scheme in [23] entails certain matrix computations, such as high-dimensional matrix inversion as part of the least squares method, which indicates there is still room for improvement in computational efficiency. In addition, an emerging class of software-based schemes utilizing machine learning has been proposed, such as in [24], [25], and [26], to detect and localize OCFs in MMCs. These methods have a low computational burden and do not require mathematical models of the MMCs. However, training the models may require extensive historical data, which can introduce significant implementation complexity, especially in high-voltage applications where hundreds of SMs are used per arm.

Another significant research gap concerns the fault modeling and estimation. The detection and localization of OCFs in many existing schemes rely on the fact that the capacitor voltage of faulty SM will deviate from those of healthy ones under OCFs conditions, such as [14], [17], [19], [21], [22], [23], [27], [28], [29], and [30]. However, to the best of the authors' knowledge, no existing works have derived a model that can quantify the actual capacitor voltage deviation induced by OCFs. Yang and Saeedifard [31] proposed detailed models for healthy capacitors' voltages and arm current after OCFs. In [22], a model for faulty SM's capacitor voltage under MMC OCFs was proposed. Deng et al. [29] proposed mathematical models for the absorbed active power of faulty and healthy SM, respectively. However, the models proposed in these works do not quantify the actual deviation in capacitor voltage (that is, the *difference* between healthy and unhealthy capacitor voltage waveforms) due to the OCFs. Concerning fault estimation, the process behind capacitor voltage deviation is very important. Many existing works utilize fault estimation to determine the magnitude of the fault, which is one of the tasks of fault diagnosis. Primarily, the estimation of faults can help to clarify the nature of actual faults and enable the operator to diagnose them. It can also help to analyze the impact of faults on the system [32]. Then, the fault estimation can be exploited to implement fault tolerant control, e.g., see [33] and [34]. Compared with traditional fault detection and isolation-based fault tolerant control, estimation-based fault tolerant control leads to a better performance since the fault information can be used for fault compensation [35]. Nonetheless, most existing FDL strategies for MMC OCFs lack fault estimation capabilities.

Motivated by the above identified issues, this article proposes a new software-based FDL scheme that simultaneously addresses the following research gaps.

1) *Lack of modeling that quantifies OCFs-induced capacitor voltage deviation:* A simplified model of OCFs-induced capacitor voltage deviation is proposed. To the best of authors' knowledge, this article is the first to propose a model that quantifies OCFs-induced capacitor voltage deviation of faulty SMs. The OCFs-induced capacitor voltage deviation, quantified by ϵ in (14), is modeled as a unique form of a small error term related to the interaction of the arm reference modulating signal and arm current. This model provides a basis for the proposed FDL scheme.
2) *Absence of fault estimation capability:* The proposed model is harnessed to estimate OCFs-induced capacitor voltage deviations. A model-based fault estimator is developed that ensures accurate and fast FDL. To estimate the OCFs for the purpose of FDL, this work utilizes a Disturbance Observer (DOB). This approach is adopted because in the proposed mathematical model, the error term representing OCFs can not be straightforwardly measured from the physical MMC plant. DOB is recognized as one of the most popular robust control tools and has been successfully applied in various domains, including automobiles, networks, and unmanned aerial vehicle [36], [37], [38]. But its potential for FDL of switch OCFs in MMCs has not yet been explored. By leveraging DOB, the proposed FDL scheme demonstrates strong robustness against measurement noise.
3) *Difficulty in maintaining both constantly low computational burden and implementation complexity:* By implementing the DOB on only one selected signature waveform for each arm, the computational burden and implementation complexity of the proposed scheme maintains very low and constant regardless of the SMs count used per arm. This feature puts both the computational burden and implementation complexity of the proposed scheme in the lowest tier among all published works for high-voltage application scenarios where hundreds of SMs are installed.

The rest of the article is organized as follows. Section II introduces the normal operating conditions and the OCFs characteristics of MMCs. The FDL scheme is proposed in Section III. The experimental results are given in Section IV. The discussions and comparative analysis are presented in Section V. Finally, Section VI concludes this article.

II. Principles and OCFs Characteristics of MMCs

A. Fundamentals of MMCs

The three-phase MMC is depicted in Fig. 1. Each phase leg of the MMC is composed of an upper arm and a lower arm, with multiple half-bridge SMs connected in series. Arm inductors L_a are placed within the arms to handle the mismatch between the sum of inserted SMs' capacitor voltages and DC link voltage at every switching instant. Each half-bridge SM includes two

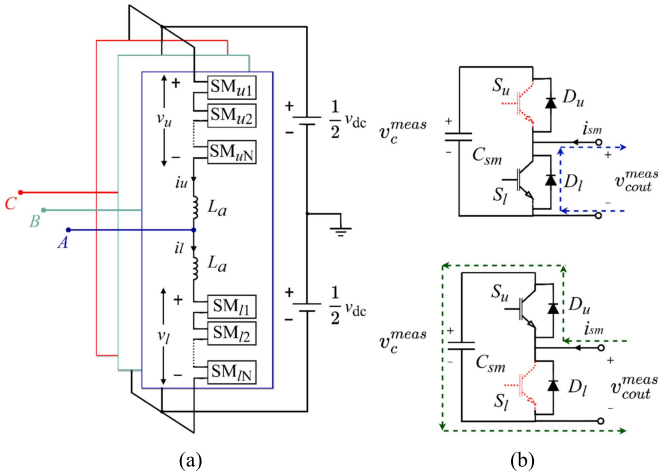

Fig. 1. Three-phase MMC topology and two types of OCFs. (a) Three-phase MMC structure. (b) Two types of OCFs in a single SM. From top to bottom: Type I and Type II OCFs.

TABLE I
CHARACTERISTICS OF SMS UNDER OCFS [23]

Condition	Scenario	i_{sm}	Operating mode	C_{sm}	v_c^{meas}
Normal	I	>0	Inserted	Charge	Increase
	II	>0	Bypassed	Bypassed	Unchanged
	III	<0	Inserted	Discharge	Decrease
	IV	<0	Bypassed	Bypassed	Unchanged
Type I OCF	I	>0	Inserted	Charge	Increase
	II	>0	Bypassed	Bypassed	Unchanged
	III	<0	Bypassed	Bypassed	Unchanged
	IV	<0	Bypassed	Bypassed	Unchanged
Type II OCF	I	>0	Inserted	Charge	Increase
	II	>0	Inserted	Charge	Increase
	III	<0	Inserted	Discharge	Decrease
	IV	<0	Bypassed	Bypassed	Unchanged

The pink background is used to highlight the affected scenarios.

IGBTs (i.e., S_u and S_l), two anti-parallel diodes (i.e., D_u and D_l), and a capacitor C_{sm}.

There are four switching scenarios within a single fundamental period of the MMC under normal conditions, resulting from the different polarities of i_{sm} and various states of S_u and S_l [39]. These scenarios are summarized in Table I. The duty cycle of each SM is defined as

$$d = \begin{cases} 1, & S_u \text{ is ON and } S_l \text{ is OFF}, \quad \text{Inserted} \\ 0, & S_u \text{ is OFF and } S_l \text{ is ON}, \quad \text{Bypassed}. \end{cases} \tag{1}$$

The waveforms of SMs' individual capacitor voltages under healthy conditions are shown in Fig. 2. Because the capacitor voltage balancing algorithm proposed in [40] is adopted, the capacitors of the SMs undergo a continuous cycle of being charged and then bypassed when i_{sm} is positive (scenarios I and II). Similarly, when i_{sm} is negative (scenarios III and IV), all SM's capacitors cyclically transition between being discharged and bypassed.

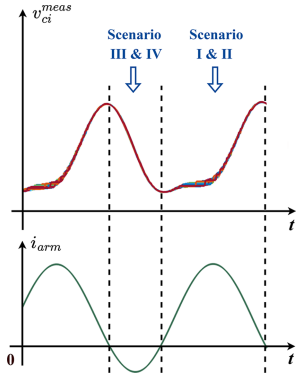

Fig. 2. SM capacitor voltages under healthy condition.

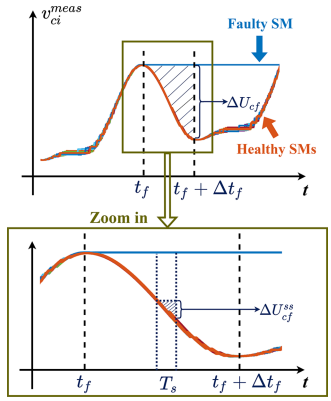

Fig. 3. SM capacitor voltages under Type I OCF during the interval for scenarios III and IV.

B. Characteristics of MMCs Under OCFs

Fig. 1(a) illustrates two possible OCFs in a single SM: Type I S_u OCF and Type II S_l OCF.

Based on the positive direction reference of i_{sm} and v_{sm} defined in Fig. 1(b), the characteristics of SM under two types of OCFs are described below and also summarized in Table I.

1) *Type I:* An OCF occurs at S_u, and does not affect scenarios I, II, IV, as indicated in Table I. However, in scenario III, the negative i_{sm} which should have flowed through C_{sm} and S_u, is instead forced to pass through D_l. The dashed line in the upper part of Fig. 1(b) illustrates the path of i_{sm} when a Type I fault occurs. Consequently, the capacitor is bypassed and unable to discharge. Therefore, the capacitor voltage of faulty SM remains unchanged during the interval for scenarios III and IV. Fig. 3 displays the waveforms of the capacitor voltages for individual SMs under a Type I OCF condition. Here, T_s represents the sampling period, t_f indicates the moment when Type I OCF becomes detectable (the beginning of the interval for scenarios III and IV) and Δt_f is the duration of the interval for scenarios III and IV. After $t = t_f$, the capacitor voltage of the unhealthy SM begins to diverge from those of healthy ones, a deviation denoted by ΔU_{cf}. The single-step deviation at each sampling instant is represented as ΔU_{cf}^{ss}.

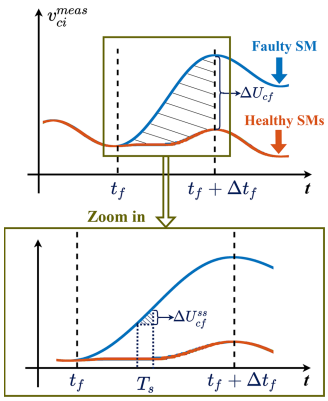

Fig. 4. SM capacitor voltages under Type II OCF during the interval for scenarios I and II.

2) *Type II:* An OCF occurs at S_l. The faulty SM will be only affected in the scenario II. The dashed line in the lower part of Fig. 1(b) illustrates the path of i_{sm} in this scenario. It can be seen that positive i_{sm} flows through D_u and C_{sm} instead of S_l. Consequently, the capacitor is charged and unable to be bypassed. Therefore, the capacitor voltage of the faulty SM keeps increasing during the interval for scenarios I and II. Fig. 4 displays the waveforms of the capacitor voltages for individual SMs under a Type II OCF condition. In this figure, t_f indicates the moment when Type I OCF becomes detectable (the beginning of the interval for scenarios I and II) and Δt_f is the duration of the interval for scenarios I and II. From the moment t_f, the capacitor voltage of unhealthy SM begins to diverge from those of healthy ones, quantified by ΔU_{cf}.

It can be concluded from Figs. 3 and 4 that the capacitor voltage of the faulty SM becomes the highest among all the individual capacitor voltages under either type of OCFs, which offers a basis for the selected signature waveform in the following.

III. Proposed FDL Scheme

In this section, a unique and simplified model for the SM capacitor voltage with OCFs-induced deviation is introduced first, and then the proposed model informed estimation-based FDL scheme is proposed. The flowchart of the entire FDL scheme is shown in Fig. 5.

A. Simplified Model for SM Capacitor Voltage Deviation That Captures OCFs Characteristics

In this section, a simplified model for SM capacitor voltage for MMCs that preserves OCFs characteristics is proposed. Unlike the MMC SM capacitor voltage model based on the duty cycle of each SM utilized in [19] and [22], the proposed capacitor voltage model in this article is based on the time-averaged arm-level reference modulating signal. The utilization of this time-averaged arm-level reference modulating signal allows for the derivation of OCFs model as a unique form of a small error term related to the interaction of the arm reference modulating signal and arm current.

The time-averaged arm modulating reference of MMCs, m_{ref}, typically generated based on the output current control such as the active power, reactive power, and dc-link voltage regulation [41], can be expressed by

$$m_{ref}(t) = \frac{1}{2} \pm \frac{\mathrm{M}}{2} cos(2\pi f t + \varphi) + \Delta m \tag{2}$$

where φ is the arm voltage phase angle, f is the fundamental frequency of the system, $\mathrm{M} \in [0, 1]$ is the modulation index, and Δm includes all the compensation components, such as dc-link voltage regulation, circulating current suppression and so on.

When using a time-averaged arm model, the relationship between SM capacitor voltage can be expressed as

$$\frac{dv_{ci}^{idl}(t)}{dt} = \frac{m_{ref}(t)}{C_{sm}} i_{arm}(t) \tag{3}$$

where v_{ci}^{idl} is the ideal SM capacitor voltage, C_{sm} is the capacitance of an individual SM, and i_{arm} is arm current. Then, (3) can be discretized as

$$v_{ci}^{idl}(k+1) = \frac{T_s}{C_{sm}} \cdot m_{ref}(k) \cdot i_{arm}(k) + v_{ci}^{idl}(k) \tag{4}$$

where k denotes sampling instant.

However, in the practical implementation, m_{ref} will be compared with carriers to generate gating pulses to control MMC. Due to the limitations imposed by the switching frequency, the measured individual capacitor voltages can not be identical to the ideal SM capacitor voltage described in (4). The set of all the measured individual capacitor voltages at each sampling instant is expressed as

$$v_c^{meas}(k) = \{v_{c1}^{meas}(k), v_{c2}^{meas}(k), \ldots, v_{ci}^{meas}(k), \ldots\}. \tag{5}$$

By introducing a disturbance term ϵ to the measured SM capacitor voltage based on (4), the following equation can be obtained:

$$v_{ci}^{meas}(k+1) = \frac{T_s}{C_{sm}} \cdot m_{ref}(k) \cdot i_{arm}(k) + v_{ci}^{meas}(k) + \epsilon(k) \tag{6}$$

where $v_{ci}^{meas}(k)$ is measured SM capacitor voltage at sampling instant k.

In this article, (6) is proposed as a general and simplified mathematical model for the capacitor voltage of any single SM, with the error term ϵ representing the mismatches under the healthy condition or the fault characteristics under OCFs condition. To derive different models of ϵ under healthy and OCFs conditions, we assume that (6) represents the measured capacitor voltage of any single SM. By considering this SM as either healthy or experiencing OCFs, (6) can be subtracted by the (healthy or faulty) equation of the measured capacitor voltage of the same SM, respectively. This approach allows for the derivation of different models of ϵ under healthy or OCFs conditions.

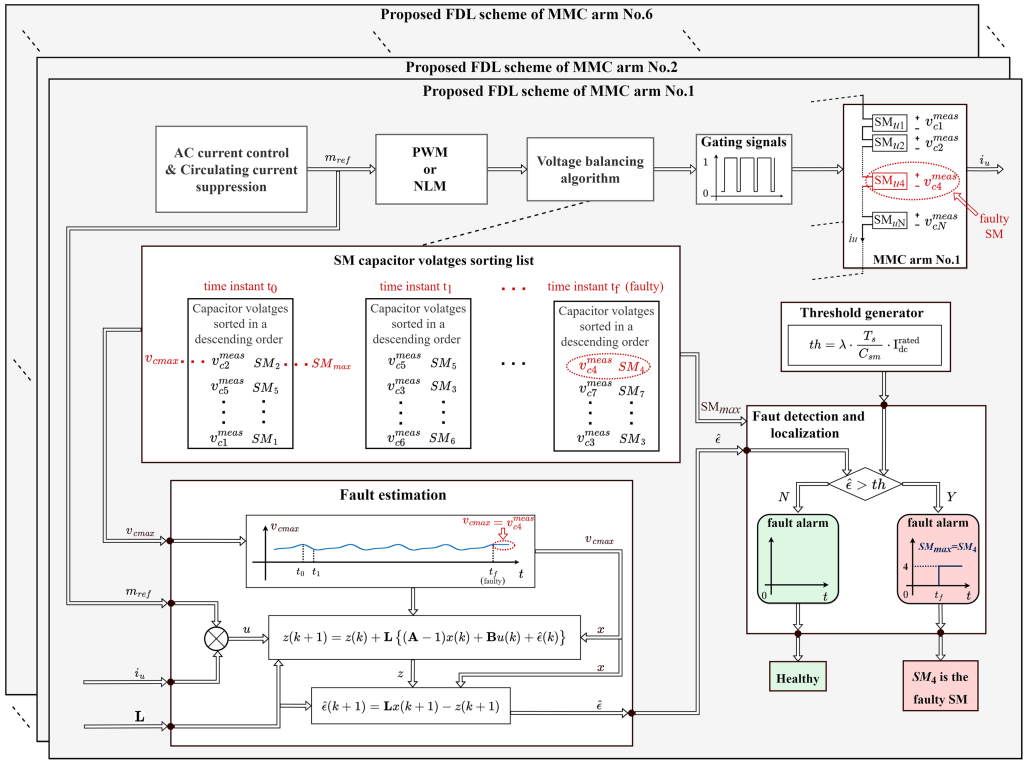

Fig. 5. Overall diagram of the proposed FDL scheme. The diagram illustrates an example of the FDL for the fourth SM of upper arm (SM_{u4}) with Type I OCF.

For the healthy condition, the measured SM capacitor voltages can be expressed as

$$v_{ci}^{meas}(k+1) = \frac{T_s}{C_{sm}} \cdot d(k) \cdot i_{arm}(k) + v_{ci}^{meas}(k) \tag{7}$$

where d is the duty cycle defined in (1). Then, the following equation can be obtained by subtracting (7) from (6) to derive the model of ϵ under healthy condition:

$$\epsilon(k) = \frac{T_s}{C_{sm}} \cdot (d - m_{ref}) \cdot i_{arm}. \tag{8}$$

For the Type I OCF condition, as presented in Section II-B and Fig. 3, under Type I OCF the capacitor voltage of faulty SM remains unchanged during the interval for scenarios III and IV. Therefore, the measured capacitor voltage can be expressed as

$$v_{ci}^{meas}(k+1) = v_{ci}^{meas}(k). \tag{9}$$

Therefore, ϵ under Type I OCF can be obtained from the subtraction of the following equations:

$$\begin{cases} v_{ci}^{meas}(k+1) = v_{ci}^{meas}(k) \\ v_{ci}^{meas}(k+1) = \frac{T_s}{C_{sm}} \cdot m_{ref}(k) \cdot i_{arm}(k) + v_{ci}^{meas}(k) + \epsilon(k). \end{cases} \tag{10}$$

For the Type II OCF condition, as presented in Section II-B and Fig. 4, under Type II OCF, the capacitor voltage of the faulty SM keeps increasing during the interval for scenarios I and II. Therefore, the measured capacitor voltage can be expressed as

$$v_{ci}^{meas}(k+1) = \frac{T_s}{C_{sm}} \cdot i_{arm}(k) + v_{ci}^{meas}(k). \tag{11}$$

Hence, the error term ϵ under Type II OCF can be obtained from the subtraction of the following equations:

$$\begin{cases} v_{ci}^{meas}(k+1) = \frac{T_s}{C_{sm}} \cdot i_{arm}(k) + v_{ci}^{meas}(k) \\ v_{ci}^{meas}(k+1) = \frac{T_s}{C_{sm}} \cdot m_{ref}(k) \cdot i_{arm}(k) + v_{ci}^{meas}(k) + \epsilon(k). \end{cases} \tag{12}$$

Considering all the scenarios mentioned in (8), (10), and (12), the measured SM capacitor voltage with OCFs characteristics can be finally obtained as

$$v_{ci}^{meas}(k+1) = \frac{T_s}{C_{sm}} \cdot m_{ref}(k) \cdot i_{arm}(k) + v_{ci}^{meas}(k) + \epsilon(k) \tag{13}$$

where

$$\epsilon(k) = \begin{cases} \frac{T_s}{C_{sm}} \cdot (d - m_{ref}) \cdot i_{arm}, & \text{healthy} \\ \frac{T_s}{C_{sm}} \cdot (-m_{ref}) \cdot i_{arm}, & \text{under Type I OCF} \\ \frac{T_s}{C_{sm}} \cdot (1 - m_{ref}) \cdot i_{arm}, & \text{under Type II OCF.} \end{cases} \tag{14}$$

This way, the proposed model described by (13) can represent the measured capacitor voltage of any single SM under either healthy or OCFs conditions. The error term ϵ described in (14) is the important simplified mathematical model for OCFs-induced capacitor voltage deviation proposed in this article. Under healthy conditions, (13) can represent the measured capacitor voltage of a single SM and ϵ is a small error term representing model mismatches. Under either type of OCFs condition, (13)

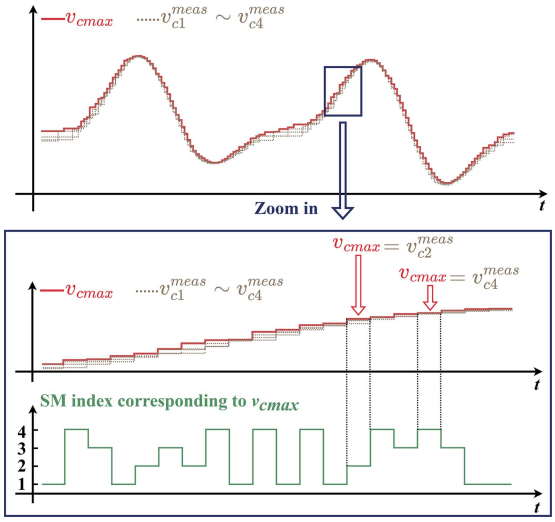

Fig. 6. Waveforms of $v_{c1}^{meas} \sim v_{c4}^{meas}$ & v_{cmax} and the SM index corresponding to v_{cmax} under normal condition. In the upper part, v_{cmax} is shown with the solid line, and $v_{c1}^{meas} \sim v_{c4}^{meas}$ are shown with dotted lines. The lower part shows the SM index corresponding to v_{cmax}.

can represent the measured capacitor voltage of the faulty SM and ϵ represents the single-step OCFs-induced change, ΔU_{cf}^{ss}.

B. Model of Selected Signature Signal for FDL

For our analysis, the maximum individual capacitor voltage is needed at each sampling instant, which is defined as

$$v_{cmax}(k) = \max\left(v_c^{meas}(k)\right). \tag{15}$$

As an example, waveforms of v_{cmax} and $v_{c1}^{meas} \sim v_{c4}^{meas}$ are presented in Fig. 6 for an MMC with $N = 4$ SMs per arm. As explained in [23], v_{cmax} presents similar periodical patterns as individual SM capacitor voltages under normal conditions. But the faulty SM's capacitor voltage waveform under both types of OCFs will manifest certain characteristics that deviate from the normal condition, and such OCFs-induced changes become dominant in v_{cmax} after the fault occurrence.

Note that (13) can represent the measured capacitor voltage of a single SM under both the healthy condition and the faulty conditions. Also, the term ϵ is used to represent the OCFs-induced voltage deviation under either type of OCFs. Since (13) is a general form applicable to the measured capacitor voltage of every single SM, it can be applied to all the elements of the set in (5). By expressing the set in (5) in the form of (13) and taking the maximum on both sides of the equation, the following equation can be derived:

$$v_{cmax}(k+1) = \frac{T_s}{C_{sm}} \cdot m_{ref}(k) \cdot i_{arm}(k) + v_{cmax}(k) + \epsilon(k). \tag{16}$$

Accordingly, v_{cmax} can be further modeled as in a state-space form as

$$\begin{cases} x(k+1) = \mathbf{A}x(k) + \mathbf{B}u(k) + \epsilon(k) \\ y(k) = \mathbf{C}x(k) \end{cases} \tag{17}$$

where $x(k) = v_{cmax}(k)$, $u(k) = m_{ref}(k) \cdot i_{arm}(k)$, $\mathbf{A} = 1$, $\mathbf{B} = \frac{1}{C_{sm}} \cdot T_s$, $\mathbf{C} = 1$, $\epsilon(k)$ is the defined in (14).

It should be noted that the sorting for $v_c^{meas}(k)$ does not require any extra calculations as it is obtained from the capacitor voltage balancing algorithm directly [40].

C. Model Informed Estimation of OCFs Based on DOB

The mathematical model of error term proposed in (14) manifests distinct characteristics under the healthy and different OCFs conditions, which makes it a suitable indicator for detecting the OCFs, and at the same time capturing the fault characteristics. However, the mathematical model cannot be directly applied for practical FDL purposes. The actual ϵ must be obtained from the physical MMC plant to facilitate FDL. Since the actual ϵ cannot be straightforwardly measured, a Disturbance Observer (DOB) is employed to estimate ϵ.

DOB has been one of the most widely used tools for robust control due to its simplicity, flexibility, and efficacy, since it was proposed by Ohishi [42] (1983). In DOB-based robust control, internal and external disturbances are estimated by using identified dynamics and measurable states of plants, and the robustness of systems is simply achieved by compensating the estimations of disturbances.

For OCFs estimation, a discrete-time DOB proposed in [43] can be implemented to estimate ϵ in (17). The disturbance is assumed to be unknown but slowly time-varying. The estimation of ϵ is achieved by using an auxiliary variable and the observer is designed as follows:

$$\begin{cases} \hat{\epsilon}(k) = \mathbf{L}x(k) - z(k) \\ z(k+1) = z(k) + \mathbf{L}\left\{\left(\mathbf{A} - I_n\right)x(k) + \mathbf{B}u(k) + \hat{\epsilon}(k)\right\} \end{cases} \tag{18}$$

where $\hat{\epsilon}$ represents the estimation of ϵ, $\mathbf{L}$ represents the observer gain of DOB to be tuned, and z represents the auxiliary variable. For (18), $\mathbf{A} = 1$, so the following equation is obtained:

$$z(k+1) = z(k) + \mathbf{L}\left\{\mathbf{B}u(k) + \hat{\epsilon}(k)\right\}. \tag{19}$$

Then, the estimation error of disturbance, $\tilde{\epsilon}(k) = \epsilon(k) - \hat{\epsilon}(k)$, can be derived as

$$\begin{aligned} \tilde{\epsilon}(k+1) &= \epsilon(k+1) - \hat{\epsilon}(k+1) \\ &= \epsilon(k+1) - \left[\mathbf{L}x(k+1) - z(k+1)\right] \\ &= \epsilon(k+1) - \mathbf{L}\left[\mathbf{A}x(k) + \mathbf{B}u(k) + \epsilon(k)\right] \\ &\quad + z(k) + \mathbf{L}\left[\left(\mathbf{B}u(k) + \hat{\epsilon}(k)\right]\right. \\ &= \epsilon(k+1) - \left[\mathbf{L}x(k) - z(k)\right] - \mathbf{L}\left[\epsilon(k) - \hat{\epsilon}(k)\right] \\ &= \epsilon(k+1) - \epsilon(k) + \epsilon(k) - \hat{\epsilon}(k) - \mathbf{L}\left[\epsilon(k) - \hat{\epsilon}(k)\right] \\ &= (1 - \mathbf{L})\tilde{\epsilon}(k) + \Delta\epsilon(k+1) \end{aligned} \tag{20}$$

where $\Delta\epsilon(k+1) = \epsilon(k+1) - \epsilon(k)$. Equation (20) shows the estimation error will converge to zero if $|1 - \mathbf{L}| < 1$ and $\Delta\epsilon(k+1) = 0$, which means the unknown disturbance should ideally be a constant or slowly time varying bias.

To detect and localize OCFs rapidly and accurately, the implementation frequency of the FDL algorithm, f_{fdl}, can be chosen as tens of kHz. Also, in the practical medium and high voltage MMCs, the order of C_{sm} is around several mF [44], [45]. Therefore, the order of magnitude of $\frac{T_s}{C_{sm}}$ is usually a

small positive fraction less than one; consequently ϵ is a small bounded value compared with the order of v_{cmax}. Therefore, $\Delta\epsilon$ is regarded as a small value at each sampling instant. Thus, the approximation $\Delta\epsilon \approx 0$.

The DOB is able to give a satisfactory estimation for the actual disturbance but with a certain delay. The delay in the estimation can be further decreased by increasing the gain $\mathbf{L}$. But increasing $\mathbf{L}$ results in more noise contamination in the estimated disturbance. Hence, the gain $\mathbf{L}$ can be chosen by considering the tradeoff between the estimation performance and the noise effect [43].

If considering SM capacitance variation as ΔC, the variation in observer can be expressed as $\Delta B = T_s \cdot (\frac{1}{C_{sm}} - \frac{1}{C_{sm}+\Delta C})$. Rederiving (20) with this variation results in an additional term $\mathbf{L}\Delta B u(k)$ that appears in $\Delta\epsilon(k+1)$, such that $\Delta\epsilon(k+1) = \epsilon(k+1) - \epsilon(k) + \mathbf{L}\Delta B u(k)$. In practice, SM capacitance variation can be around 10%, and as mentioned C_{sm} is several mF. As a result, the $\mathbf{L}\Delta B u(k)$ remains a small, bounded value compared to the magnitude of v_{cmax}. For selecting $\mathbf{L}$, practical applications involve noises, so $\mathbf{L}$ should be selected as a small value to filter out noise. When a small $\mathbf{L}$ is selected, $\mathbf{L}\Delta B u(k)$ becomes negligible, still ensuring that $\Delta\epsilon \approx 0$. Thus, the selection of $\mathbf{L}$ for noise filtering and robustness against SM capacitance variation aligns in the same direction.

By properly choosing the observer gain $\mathbf{L}$, the estimated disturbance term $\hat{\epsilon}$ will converge to the actual ϵ, effectively filtering out measurement noise. As indicated by (14), the value of actual ϵ changes when OCFs occur. Since $\hat{\epsilon}$ can track actual ϵ, those OCFs-induced change will also be reflected in $\hat{\epsilon}$. Therefore, the error estimation $\hat{\epsilon}$ can serve as the fault indicating signal to detect and localize the OCFs when compared against a predetermined threshold.

D. Design of Threshold and FDL

Informed by the proposed OCFs model in (14), the threshold is designed as

$$th = \lambda \cdot \frac{T_s}{C_{sm}} \cdot \mathrm{I}_{\mathrm{dc}}^{\mathrm{rated}} \tag{21}$$

where λ is introduced as an adjusting coefficient, $\mathrm{I}_{\mathrm{dc}}^{\mathrm{rated}}$ is the rated dc current, and $\frac{T_s}{C_{sm}}$ is introduced as a scaling factor to make sure the threshold is in the same order of magnitude as ΔU_{cf}^{ss}.

For the fault localization, as mentioned in Section III-B, once the OCF is detected, the values of v_{cmax} after OCF must correspond to the faulty SM. Since all the SMs are sorted according to their capacitor voltages in descending order at each time instant, the first one listed in the sorting result will be the faulty SM. Experimental studies are conducted to validate and demonstrate the performance of the proposed FDL.

IV. Experimental Verification

The effectiveness of the proposed FDL scheme is verified on a lab-scale single-phase MMC prototype constructed using real-time controllers and half-bridge SMs from Imperix. The experimental setup is shown in Fig. 7 and the circuit parameters

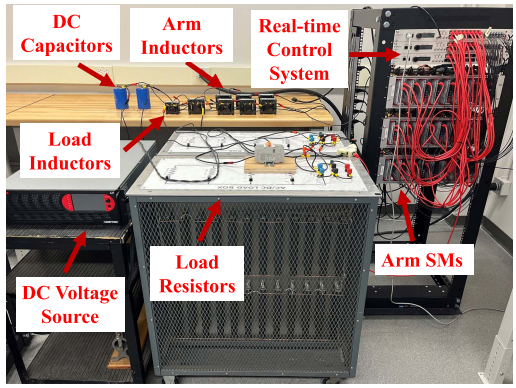

Fig. 7. Experimental setup of the single-phase MMC.

TABLE II
Experiment Parameters

MMC Parameters	
Rated apparent power, S	1.6 kVA
Power factor	0.92
Rated dc voltage, V_{dc}	260 V
SM count per arm, N	10
SM capacitance, C_{sm}	5 mF
DC bus capacitance, C_{dc}	4.7 mF
Arm inductance, L_a	6 mH
AC-side inductance, L_s	3 mH
AC-side resistance, R_s	5.2 & 10.4 Ω
Fundamental frequency, f	60 Hz
Sampling frequency, f_s	40 kHz
FDL Parameters	
Observer gain, $\mathbf{L}$	0.08
Adjusting coefficient, λ	0.4
Sampling frequency, f_{fdl}	10 kHz

are given in Table II. There are $N = 10$ SMs within each arm. The MMC works in the inverter mode, with a 260 V dc voltage source at the dc terminals and a passive load at the ac terminals. In the experiment, the OCFs of the IGBT are achieved by blocking the IGBT's associated gating signal [15], [17], [18], [23]. For the selection of $\mathbf{L}$ in the experiment, a relatively small $\mathbf{L}$ (0.08) is chosen to enhance noise filtering effect, as measurement noises is introduced by the practical sensors.

A. Case 1: Type I OCF

In this case, the effectiveness of the proposed scheme in modeling, estimation and FDL of single Type I OCF (occurring in SM_{u1} at 0.8 s) is validated. As mentioned in Section II-B, we define the actual OCFs-induced capacitor voltage deviation as ΔU_{cf} and the single-step OCFs-induced capacitor voltage deviation as ΔU_{cf}^{ss}. Equations (14) and (18) provide modeling and estimation for ΔU_{cf}^{ss}. Since the integral of ΔU_{cf}^{ss} over Δt_f is ΔU_{cf}, we can further validate that the integral of ϵ from (14) and $\hat{\epsilon}$ from (18) over Δt_f can also track ΔU_{cf}. In this case, ϵ_int denotes the integral of ϵ over the duration of the interval

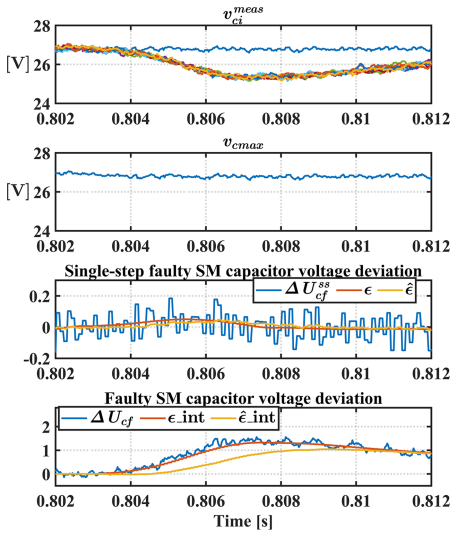

Fig. 8. Experimental results of fault modeling and estimation under Type I OCF occurred in upper arm SM_1 at 0.8 s.

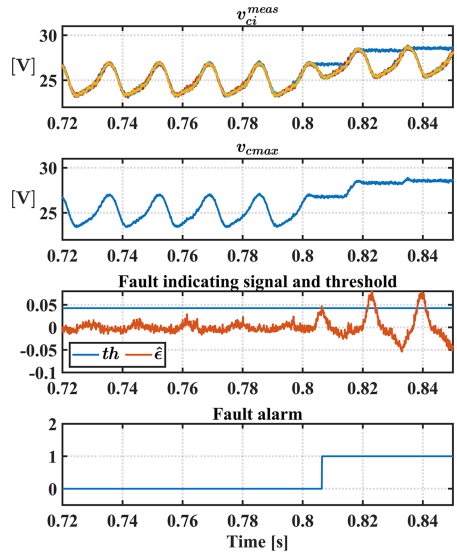

Fig. 9. Experimental results of FDL under Type I OCF occurred in upper arm SM_1 at 0.8 s. From top to bottom, the waveforms are individual capacitor voltages, v_{cmax}, $\hat{\epsilon}$ and th, and fault alarm.

for scenarios III and IV, which can be defined as

$$\epsilon\_\text{int} = \int_{t_f}^{t_f+\Delta t_f} \epsilon \, d\tau. \tag{22}$$

$\hat{\epsilon}$_int denotes the integral of $\hat{\epsilon}$, which can be defined as

$$\hat{\epsilon}\_\text{int} = \int_{t_f}^{t_f+\Delta t_f} \hat{\epsilon} \, d\tau. \tag{23}$$

The effectiveness of OCFs' modeling and estimation is verified in Fig. 8. After the Type I OCF occurs at 0.8 s, the faulty SM capacitor voltage deviates from healthy ones rapidly as shown in the first subplot. The second subplot illustrates that the Type I OCF-induced capacitor voltage deviation of the faulty SM becomes dominant in v_{cmax} after the fault occurrence. The third subplot of Fig. 8 verifies that when OCF happens, the disturbance term ϵ given in the simplified model (14) can accurately model the single-step faulty SM capacitor voltage deviation ΔU_{cf}^{ss}. Furthermore, the estimated disturbance $\hat{\epsilon}$ tracks ΔU_{cf}^{ss} with a small delay. To further validate the effectiveness of OCFs' modeling and estimation, the faulty SM capacitor voltage deviation ΔU_{cf} is calculated as the difference between the measured v_{c1}^{meas} (faulty) and v_{c3}^{meas} (healthy) of the upper arm. The forth subplot of Fig. 8 verifies that when an OCF occurs, the integral error term ϵ_int defined in (22) can accurately represent ΔU_{cf}, which can be estimated using the DOB-based estimator with a small delay.

The effectiveness of FDL is verified in Fig. 9. In the proposed FDL scheme, the estimated disturbance $\hat{\epsilon}$ serves as the fault indicating signal, compared with the threshold th designed in (21). It can be seen that when the healthy MMC operates at a steady state before the OCF happens, the estimated fault indicator $\hat{\epsilon}$ remains below th as shown in the third subplot. After the Type I fault occurs at 0.8 s, $\hat{\epsilon}$ increases and surpasses th shortly after OCF happens. At the sampling instant when the fault is detected, SM_{u1}, which ranks first in the sorting algorithm, is determined as the faulty SM. The fault alarm of the upper arm steps from zero to five, indicating OCF happens in SM_{u1} as shown in the third subplot. Type I OCF can be detected and localized at 0.8064 s, which is 6.4 ms after OCF occurs.

B. Case 2: Type II OCF

In this case, the effectiveness of the proposed scheme in modeling, estimation, and FDL of single Type II fault (occurring in SM_{l9} at 0.8 s) is validated. In this case, ϵ_int denotes the integral of ϵ and $\hat{\epsilon}$_int denotes the integral of $\hat{\epsilon}$ over the duration of the interval for scenarios I and II.

The effectiveness of OCFs' modeling and estimation is verified in Fig. 10. After the Type II OCF occurs at 0.8 s, the faulty SM capacitor voltage deviates from healthy ones rapidly as shown in the first subplot. The second subplot illustrates that the Type II OCF-induced capacitor voltage deviation of the faulty SM becomes dominant in v_{cmax} after the fault occurrence. The third subplot of Fig. 10 verifies that when OCF happens, ϵ can accurately model ΔU_{cf}^{ss}, and $\hat{\epsilon}$ tracks ΔU_{cf}^{ss} with a small delay.To further validate the effectiveness of OCFs' modeling and estimation, the faulty SM capacitor voltage deviation ΔU_{cf} is calculated as the difference between the measured v_{c9}^{meas} (faulty) and v_{c10}^{meas} (healthy) of the lower arm. The forth subplot of Fig. 10 verifies that when an OCF fault occurs, the integral error term ϵ_int defined in (22) can accurately represent ΔU_{cf}, which can be estimated using the DOB-based estimator with a small delay.

The effectiveness of FDL is verified in Fig. 11. After the Type II OCF occurs at 0.8s, the estimated fault indicator $\hat{\epsilon}$ increases and surpasses th shortly after OCF happens. At the sampling instant when the fault is detected, SM_{l9}, which ranks first in the sorting algorithm, is determined as the faulty SM. The fault alarm of the upper arm steps from zero to nine, indicating OCF happens in SM_{l9} as shown in the third subplot. Type II

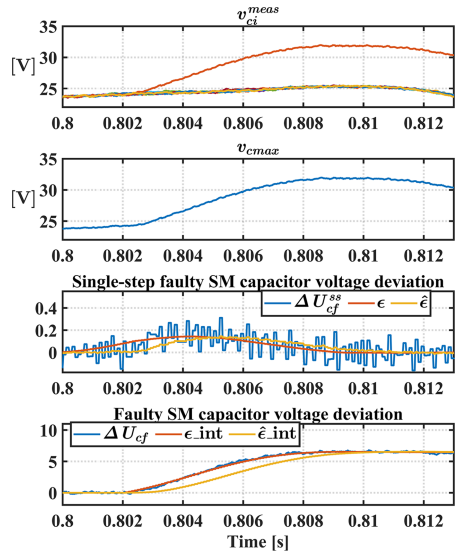

Fig. 10. Experimental results of fault modeling and estimation under Type II OCF occurred in lower arm SM_9 at 0.8 s.

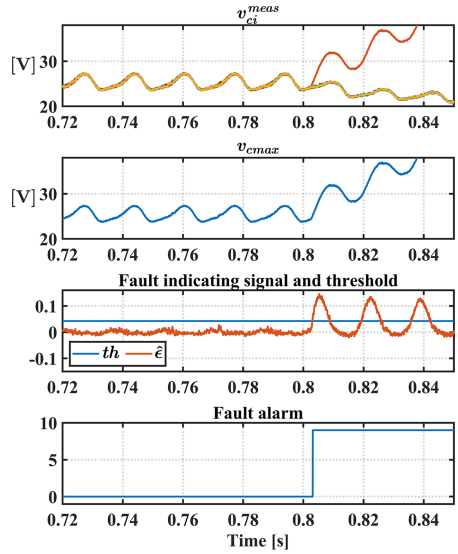

Fig. 11. Experimental results of FDL under Type II OCF occurred in lower arm SM_9 at 0.8 s. From top to bottom, the waveforms are individual capacitor voltages, v_{cmax}, $\hat{\epsilon}$ and th, and fault alarm.

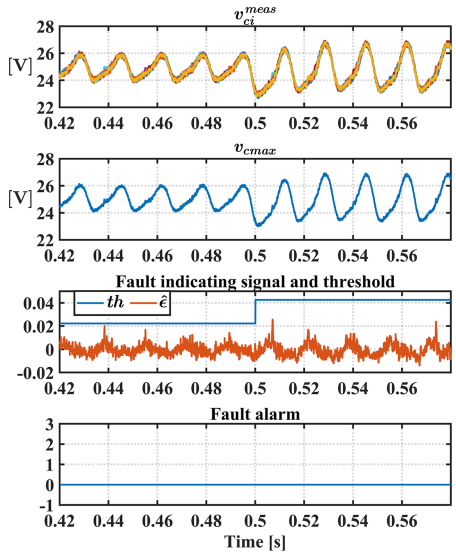

Fig. 12. Experimental results under load-step up change occurred at 0.5 s. From top to bottom, the waveforms are individual capacitor voltages, v_{cmax}, $\hat{\epsilon}$ and th, and fault alarm.

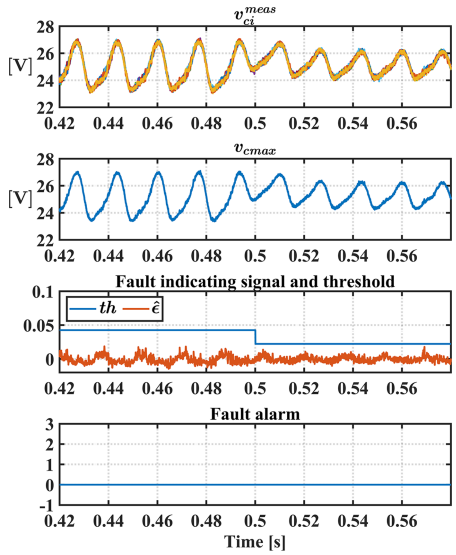

Fig. 13. Experimental results under load-step down change occurred at 0.5 s. From top to bottom, the waveforms are individual capacitor voltages, v_{cmax}, $\hat{\epsilon}$ and th, and fault alarm.

OCF can be detected and localized at 0.8031 s, which is 3.1 ms after OCF occurs.

C. Case 3: Load Changes

In this case, the robustness of the proposed FDL scheme against load current changes is validated.

The results for load step-up change are shown in Fig. 12, the load resistance is changed from 10.4 to 5.2 Ω at 0.5 s. The results for load step-down change are shown in Fig. 13, the load resistance is changed from 5.2 to 10.4 Ω at 0.5 s. It can be seen that $\hat{\epsilon}$ stays below th under both load step-up and load step-down changes. Hence no false alarms are triggered, which demonstrates that the proposed scheme is robust against load changes.

D. Case 4: Simultaneous OCFs in Multiple SMs

In this case, the effectiveness of the proposed scheme in FDL of simultaneous double Type I OCFs (occurring in SM_3 & SM_4), and simultaneous double Type II OCFs (occurring in SM_9 & SM_{10}) is validated. As analyzed in [23], simultaneous double OCFs-induced changes will become dominant in the waveforms consisting of the highest and the second highest individual capacitor voltage, which can be denoted as v_{cmax1} and v_{cmax2} . Therefore, to detect and localize simultaneous double OCFs, the

TABLE III
COMPARISON OF FDL SCHEMES

Schemes	Signals needed	Computation burden	FDL time of single OCF	Capability of fault estimation	Circuit parameters based	Verification of FDL for simultaneous multiple OCFs
[15]	Arm current and SMs' capacitor voltages	$O(N^2)$	Within three fundamental cycles	No	Yes	No
[14]	Arm current and SMs' capacitor voltages	$O(N)$	Within eight fundamental cycles	No	Yes	No
[47]	Arm current and SMs' capacitor voltages	$O(N)$	Within eight fundamental cycles	No	Yes	No
[48]	Arm current and SMs' capacitor voltages	$O(N)$	Within two fundamental cycles	No	Yes	No
[17]	Arm current and SMs' capacitor voltages	$O(N^2)$	Within one fundamental cycle	No	Yes	No
[49]	SMs' capacitor voltages	$O(N)$	One fundamental cycle ~ Eight fundamental cycles	No	No	No
[21]	Arm current and SMs' capacitor voltages	$O(N)$	Within one fundamental cycle	No	Yes	No
[23]	SMs' capacitor voltages	$O(1)$	Within two fundamental cycles	No	No	Yes
Proposed Scheme	Arm current and SMs' capacitor voltages	$O(1)$	Within one fundamental cycle	Yes	Yes	Yes

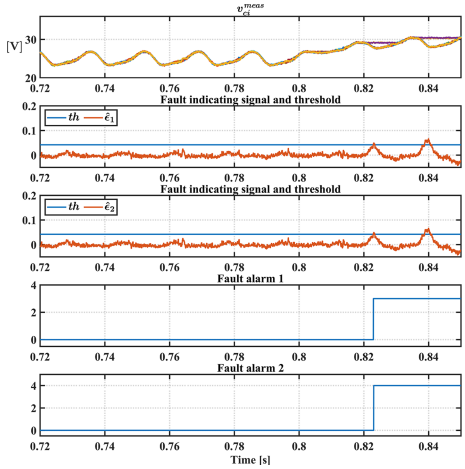

Fig. 14. Experimental results under simultaneous multiple Type I OCFs occurred in upper arm SM_3 & SM_4 at 0.8 s. From top to bottom, the waveforms are individual capacitor voltages, $\hat{\epsilon}_1$, $\hat{\epsilon}_2$, th, and fault alarms.

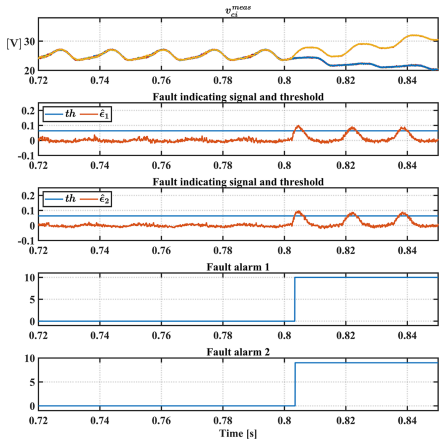

Fig. 15. Experimental results under simultaneous multiple Type II OCFs occurred in lower arm SM_9 & SM_{10} at 0.8 s. From top to bottom, the waveforms are individual capacitor voltages, $\hat{\epsilon}_1$, $\hat{\epsilon}_2$, th, and fault alarms.

proposed FDL scheme is implemented on these two waveforms simultaneously.

Simultaneous double Type I OCFs are presented in the first experiment of case 4. As shown in Fig. 14, both OCFs occur at 0.8 s. The capacitor voltages of SM_3 and SM_4 both deviate from the remaining healthy ones when OCFs occurs. $\hat{\epsilon}_1$ surpasses th, and SM_3 is determined as the faulty SM. At almost the same time when SM_3 is detected and localized, $\hat{\epsilon}_2$ surpasses th, and the faulty SM_4 is also detected and localized. Both these two faulty SMs are successfully detected and localized at 0.823s. The FDL time is 23 ms. For the second experiment of case 4, simultaneous double Type II OCFs occur at 0.8 s. It can be seen in Fig. 15 that both faulty SMs are successfully detected and localized within 3.4 ms.

V. DISCUSSION AND COMPARISONS

A comparison of several software-based FDL schemes is presented in Table III. For computational efficiency, the similar quantification method adopted in [21] based on Big O notation is also adopted in this article. $O(N^2)$ denotes that the computation burden is a quadratic function of N, and $O(N)$ denotes the computation burden is a linear function of N. As mentioned, most software-based methods typically implement their computations on all individual SMs at each sampling instant. As the SM count per arm significantly increases, so does the computational burden. In contrast, the proposed scheme in this article implements one observer on one specific signature waveform per arm, v_{cmax}, instead of iterating through all the SMs at each sampling instant. Consequently, the computational burden of the proposed scheme remains very low and independent of N which can be denoted as $O(1)$. Regarding the scheme proposed in [23], its computational requirements also do not increase with N, but it imposes computation on one more waveform and entails certain matrix computations. Compared with [23], the computational burden of the work proposed in this article is much lower.

In terms of FDL time, the proposed scheme demonstrates the ability to detect and localize the OCF within one fundamental

cycle. Table III provides a comparison of the FDL time for detecting and localizing single OCF with methods proposed in other papers. It can be seen that the proposed scheme has the shortest FDL time. It should be noted that the FDL time can only be roughly compared, as it depends on various factors such as hardware parameters, operating conditions, and circuit parameters [46].

VI. Conclusion

This article proposed a model informed estimation-based FDL scheme for switch OCFs of MMCs. This scheme effectively detected and localized OCFs by capitalizing on a novel model that is able to quantify the expected deviation in capacitor voltage by considering only the time-averaged arm reference modulating signal and the arm current. Based on the theoretical analysis and verification results, the proposed scheme was the only one who has the following distinctive features: 1) the proposed simplified modeling can accurately model the actual single-step OCFs-induced capacitor voltage deviation; 2) the proposed DOB-based model informed method provides a satisfactory estimation for OCFs; 3) and by utilizing DOB on only one selected signature waveform, v_{cmax}, there is no need to execute the FDL algorithm on all individual SMs at each sampling instant, thus keeping the computation burden and implementation complexity very low and constant as the SMs count per arm increases. The proposed scheme also had some general advantages, such as relatively short FDL time, robustness against load change and measurement noises. Its efficacy was verified by experimental results obtained from a lab-scale eleven-level MMC prototype.

References

[1] G. J. Kish, "On the emerging class of non-isolated modular multilevel DC–DC converters for DC and hybrid AC–DC systems," *IEEE Trans. Smart Grid*, vol. 10, no. 2, pp. 1762–1771, Mar. 2019.

[2] Y. Chen, S. Zhao, Z. Li, X. Wei, and Y. Kang, "Modeling and control of the isolated DC–DC modular multilevel converter for electric ship medium voltage direct current power system," *IEEE Trans. Emerg. Sel. Topics Power Electron.*, vol. 5, no. 1, pp. 124–139, Mar. 2017.

[3] G. J. Kish, M. Ranjram, and P. W. Lehn, "A modular multilevel DC/DC converter with fault blocking capability for HVDC interconnects," *IEEE Trans. Power Electron.*, vol. 30, no. 1, pp. 148–162, Jan. 2015.

[4] Q. Chen, R. Li, and X. Cai, "Analysis and fault control of hybrid modular multilevel converter with integrated battery energy storage system," *IEEE Trans. Emerg. Sel. Topics Power Electron.*, vol. 5, no. 1, pp. 64–78, Mar. 2017.

[5] Y. Jin et al., "A dual-layer back-stepping control method for lyapunov stability in modular multilevel converter based STATCOM," *IEEE Trans. Ind. Electron.*, vol. 69, no. 3, pp. 2166–2179, Mar. 2022.

[6] S. Yang, A. Bryant, P. Mawby, D. Xiang, L. Ran, and P. Tavner, "An industry-based survey of reliability in power electronic converters," *IEEE Trans. Ind. Appl.*, vol. 47, no. 3, pp. 1441–1451, May/Jun. 2011.

[7] Y. Song and B. Wang, "Survey on reliability of power electronic systems," *IEEE Trans. Power Electron.*, vol. 28, no. 1, pp. 591–604, Jan. 2013.

[8] U.-M. Choi, F. Blaabjerg, and K.-B. Lee, "Study and handling methods of power IGBT module failures in power electronic converter systems," *IEEE Trans. Power Electron.*, vol. 30, no. 5, pp. 2517–2533, May 2015.

[9] Q. Xiao et al., "Review of fault diagnosis and fault-tolerant control methods of the modular multilevel converter under submodule failure," *IEEE Trans. Power Electron.*, vol. 38, no. 10, pp. 12059–12077, Oct. 2023.

[10] R. Picas, J. Zaragoza, J. Pou, and S. Ceballos, "Reliable modular multilevel converter fault detection with redundant voltage sensor," *IEEE Trans. Power Electron.*, vol. 32, no. 1, pp. 39–51, Jan. 2017.

[11] J. Wang, H. Ma, and Z. Bai, "A submodule fault ride-through strategy for modular multilevel converters with nearest level modulation," *IEEE Trans. Power Electron.*, vol. 33, no. 2, pp. 1597–1608, Feb. 2018.

[12] J. Zhang, X. Hu, S. Xu, Y. Zhang, and Z. Chen, "Fault diagnosis and monitoring of modular multilevel converter with fast response of voltage sensors," *IEEE Trans. Ind. Electron.*, vol. 67, no. 6, pp. 5071–5080, Jun. 2020.

[13] Z. Wang and L. Peng, "Grouping capacitor voltage estimation and fault diagnosis with capacitance self-updating in modular multilevel converters," *IEEE Trans. Power Electron.*, vol. 36, no. 2, pp. 1532–1543, Feb. 2021.

[14] F. Deng, Z. Chen, M. R. Khan, and R. Zhu, "Fault detection and localization method for modular multilevel converters," *IEEE Trans. Power Electron.*, vol. 30, no. 5, pp. 2721–2732, May 2015.

[15] S. Shao, A. J. Watson, J. C. Clare, and P. W. Wheeler, "Robustness analysis and experimental validation of a fault detection and isolation method for the modular multilevel converter," *IEEE Trans. Power Electron.*, vol. 31, no. 5, pp. 3794–3805, May 2016.

[16] M. Abdelsalam, M. I. Marei, and S. B. Tennakoon, "An integrated control strategy with fault detection and tolerant control capability based on capacitor voltage estimation for modular multilevel converters," *IEEE Trans. Ind. Appl.*, vol. 53, no. 3, pp. 2840–2851, May/Jun. 2017.

[17] D. Zhou, H. Qiu, S. Yang, and Y. Tang, "Submodule voltage similarity-based open-circuit fault diagnosis for modular multilevel converters," *IEEE Trans. Power Electron.*, vol. 34, no. 8, pp. 8008–8016, Aug. 2019.

[18] X. Chen, J. Liu, Z. Deng, S. Song, S. Du, and D. Wang, "A diagnosis strategy for multiple IGBT open-circuit faults of modular multilevel converters," *IEEE Trans. Power Electron.*, vol. 36, no. 1, pp. 191–203, Jan. 2021.

[19] H. Jia, Y. Deng, X. Hu, Z. Deng, and X. He, "A concurrent diagnosis method of IGBT open-circuit faults in modular multilevel converters," *IEEE Trans. Emerg. Sel. Topics Power Electron.*, vol. 11, no. 1, pp. 1021–1034, Feb. 2023.

[20] Z. Liu, L. Xiao, Q. Wang, J. Li, and Q. Wu, "Open-circuit fault diagnosis for MMC based on event-triggered and capacitor current state observation," *IEEE Trans. Circuits Syst. II: Exp. Briefs*, vol. 69, no. 2, pp. 534–538, Feb. 2022.

[21] Y. Jin et al., "A novel detection and localization approach of open-circuit switch fault for the grid-connected modular multilevel converter," *IEEE Trans. Ind. Electron.*, vol. 70, no. 1, pp. 112–124, Jan. 2023.

[22] Z. Liu, L. Xiao, X. Cao, and Z. Deng, "A faulty submodule mathematical model-based localization strategy for switch open-circuit fault of module multilevel converter," *IEEE Trans. Power Electron.*, vol. 38, no. 3, pp. 3899–3916, Mar. 2023.

[23] H. Wang, Y. Li, A. Wijesekera, G. J. Kish, and Q. Zhao, "Switch open-circuit fault detection and localization for modular multilevel converters based on signal synthesis," *IEEE Trans. Emerg. Sel. Topics Power Electron.*, vol. 11, no. 5, pp. 5391–5404, Oct. 2023.

[24] S. Kiranyaz, A. Gastli, L. Ben-Brahim, N. Al-Emadi, and M. Gabbouj, "Real-time fault detection and identification for MMC using 1-D convolutional neural networks," *IEEE Trans. Ind. Electron.*, vol. 66, no. 11, pp. 8760–8771, Nov. 2019.

[25] A. Mohammadhassani and A. Mehrizi-Sani, "Open-circuit submodule fault diagnosis in MMCs using support vector machines," *IET Generation, Transmiss. Distrib.*, vol. 16, no. 24, pp. 5015–5025, Oct. 2022.

[26] F. Deng, M. Jin, C. Liu, M. Liserre, and W. Chen, "Switch open-circuit fault localization strategy for MMCs using sliding-time window based features extraction algorithm," *IEEE Trans. Ind. Electron.*, vol. 68, no. 10, pp. 10193–10206, Oct. 2021.

[27] Z. Geng and M. Han, "Fault localization strategy for modular multilevel converters in rectifier mode under submodule switch open-circuit failure," *IEEE Trans. Circuits Syst. II: Exp. Briefs*, vol. 67, no. 12, pp. 3222–3226, Dec. 2020.

[28] M. Jin, F. Deng, C. Liu, Q. Yu, J. Zhao, and Q. Wang, "Statistical multi-faults localization strategy of switch open-circuit fault for modular multilevel converters using grubbs criterion," in *Proc. IECON 2020 46th Annu. Conf. IEEE Ind. Electron. Soc.*, Oct. 2020, pp. 5302–5307.

[29] F. Deng, Y. Chen, J. Dou, C. Liu, Z. Chen, and F. Blaabjerg, "Isolation forest based submodule open-circuit fault localization method for modular multilevel converters," *IEEE Trans. Ind. Electron.*, vol. 70, no. 3, pp. 3090–3102, Mar. 2023.

[30] S. Hamayoon, M. Hovd, and J. A. Suul, "Fault detection, localization and clearance for MMC based on indirect finite control set model predictive control," in *Proc. IEEE 32nd Int. Symp. Ind. Electron.*, Jun. 2023, pp. 1–8.

[31] Q. Yang and M. Saeedifard, "Analysis of the modular multilevel converter under single open-circuit fault in the upper active switch of a submodule," in *Proc. 2019 IEEE Appl. Power Electron. Conf. Expo.*. Mar. 2019, pp. 1817–1824.
[32] J. Chen and R. J. Patton, "Fault estimation in linear dynamic systems," *IFAC Proc. Volumes*, vol. 26, no. 2, Part 5, pp. 503–506, Jul. 1993.
[33] B. Jiang, M. Staroswiecki, and V. Cocquempot, "Fault accommodation for nonlinear dynamic systems," *IEEE Trans. Autom. Control*, vol. 51, no. 9, pp. 1578–1583, Sep. 2006.
[34] M. Rodrigues, H. Hamdi, N. BenHadj Braiek, and D. Theilliol, "Observer-based fault tolerant control design for a class of LPV descriptor systems," *J. Franklin Inst.*, vol. 351, no. 6, pp. 3104–3125, Jun. 2014.
[35] Z. Gong, D. Huang, H. U. K. Jadoon, L. Ma, and W. Song, "Sensor-fault-estimation-based tolerant control for single-phase two-level PWM rectifier in electric traction system," *IEEE Trans. Power Electron.*, vol. 35, no. 11, pp. 12274–12284, Nov. 2020.
[36] T. Bünte, D. Odenthal, B. Aksun-Güvenç, and L. Güvenç, "Robust vehicle steering control design based on the disturbance observer," *Annu. Rev. Control*, vol. 26, no. 1, pp. 139–149, Jan. 2002.
[37] K. Natori and K. Ohnishi, "A design method of communication disturbance observer for time-delay compensation, taking the dynamic property of network disturbance into account," *IEEE Trans. Ind. Electron.*, vol. 55, no. 5, pp. 2152–2168, May 2008.
[38] A. Moeini, A. F. Lynch, and Q. Zhao, "A backstepping disturbance observer control for multirotor UAVs: Theory and experiment," *Int. J. Control*, vol. 95, no. 9, pp. 2364–2378, Sep. 2022.
[39] K. Sharifabadi, L. Harnefors, H.-P. Nee, S. Norrga, and R. Teodorescu, *Design, Control and Application of Modular Multilevel Converters for HVDC Transmission Systems*. Chichester, U.K.: John Wiley & Sons, Inc., Ltd, Oct. 2016.
[40] M. Glinka and R. Marquardt, "A new AC/AC multilevel converter family," *IEEE Trans. Ind. Electron.*, vol. 52, no. 3, pp. 662–669, Jun. 2005.
[41] C. Liu, F. Deng, Q. Yu, Y. Wang, F. Blaabjerg, and X. Cai, "Submodule capacitance monitoring strategy for phase-shifted carrier pulsewidth-modulation-based modular multilevel converters," *IEEE Trans. Ind. Electron.*, vol. 68, no. 9, pp. 8753–8767, Sep. 2021.
[42] K. Ohishi, "Torque-speed regulation of DC motor based on load torque estimation," *Proc. IEEJ IPEC*, Tokyo, Japan, 1983-3, vol. 2, pp. 1209–1216, Dec. 1983.
[43] K.-S. Kim and K.-H. Rew, "Reduced order disturbance observer for discrete-time linear systems," *Automatica*, vol. 49, no. 4, pp. 968–975, Apr. 2013.
[44] S. Cui, J.-H. Lee, J. Hu, R. W. De Doncker, and S.-K. Sul, "A modular multilevel converter with a zigzag transformer for bipolar MVDC distribution systems," *IEEE Trans. Power Electron.*, vol. 34, no. 2, pp. 1038–1043, Feb. 2019.
[45] J. Peralta, H. Saad, S. Dennetiere, J. Mahseredjian, and S. Nguefeu, "Detailed and averaged models for a 401-Level MMC–HVDC system," *IEEE Trans. Power Del.*, vol. 27, no. 3, pp. 1501–1508, Jul. 2012.
[46] J. He, Q. Yang, and Z. Wang, "On-line fault diagnosis and fault-tolerant operation of modular multilevel converters — A comprehensive review," *CES Trans. Elect. Machines Syst.*, vol. 4, no. 4, pp. 360–372, Dec. 2020.
[47] B. Li, S. Shi, B. Wang, G. Wang, W. Wang, and D. Xu, "Fault diagnosis and tolerant control of single IGBT open-circuit failure in modular multilevel converters," *IEEE Trans. Power Electron.*, vol. 31, no. 4, pp. 3165–3176, Apr. 2016.
[48] Q. Yang, J. Qin, and M. Saeedifard, "Analysis, detection, and location of open-switch submodule failures in a modular multilevel converter," *IEEE Trans. Power Del.*, vol. 31, no. 1, pp. 155–164, Feb. 2016.
[49] C. Liu et al., "Fault localization strategy for modular multilevel converters under submodule lower switch open-circuit fault," *IEEE Trans. Power Electron.*, vol. 35, no. 5, pp. 5190–5204, May 2020.

Haoran Wang (Graduate Student Member, IEEE) received the B.Sc. degree in electrical engineering from the Shenyang University of Technology, Shenyang, China, in 2019. He is currently working toward the Ph.D. degree in control systems with the Department of Electrical and Computer Engineering, University of Alberta, Edmonton, AB, Canada.

His current research interests include modular multilevel converter, HVdc, fault diagnosis, and fault tolerant control.

Anjana Wijesekera (Graduate Student Member, IEEE) received the B.Sc. degree in electrical and electronic engineering from the Faculty of Engineering, University of Peradeniya, Peradeniya, Sri Lanka, in 2017. He is currently working toward the Ph.D. degree in energy systems with the Department of Electrical and Computer Engineering, University of Alberta, Edmonton, AB, Canada.

His research interests include modular multilevel converter topologies, ac–ac converters, and MMC controls.

Gregory J. Kish (Senior Member, IEEE) received the B.E.Sc. degree from the University of Western Ontario, London, ON, Canada, in 2009, and the M.A.Sc. and Ph.D. degrees from the University of Toronto, Toronto, in 2011 and 2016, respectively, all in electrical engineering. He is currently an Associate Professor with the University of Alberta, Edmonton, AB, Canada.

His research interests relate to the development and application of power electronic converter systems in electric grids.

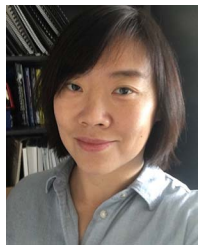

Qing Zhao (Member, IEEE) received the B.Sc. degree in control engineering from Northeastern University (NEU), Shenyang, China, and the Ph.D. degree in electrical engineering from the University of Western Ontario, London, ON, Canada, in 1993 and 1999, respectively.

She is currently a Professor with the Department of Electrical and Computer Engineering, University of Alberta, Edmonton, AB, Canada. She was a Visiting Professor with the Control Engineering Department, Universite Libre de Bruxelles, Brussels, Belgium, from August to December 2008. She held an A.v. Humboldt Research Fellowship and was a Visiting Professor with the University of Duisburg-Essen, Duisburg, Germany, from January to July 2009. Her current research interests include fault diagnosis, fault tolerant control, robust control, optimal control and estimation, machine condition monitoring, and process and data analytics.